

Modification of PLD Grown Nano TiO₂ Thin Films using 120 MeV Au Ion Irradiation

Vijay Kumar^{1*}, D.C. Agarwal², R.S. Chauhan¹

¹Deptt. Of Physics, R.B.S. College, Agra, UP, India- 282 002

²National Institute of Solar Energy, Gurugram, Haryana, India-122 003

*Corresponding Author: vijaykumar.ibs@gmail.com

ABSTRACT

Nanocrystalline TiO₂ thin films were deposited on quartz and silicon substrates using PLD method. The pristine film was exposed to 120 MeV Au ions at three different fluences ranging from 1×10^{11} to 1×10^{13} ions/cm². These films were analyzed with XRD, UV-Vis and AFM techniques to examine changes in their structural, optical, and surface morphological properties. The XRD results indicate that the pristine film is polycrystalline in nature and the irradiation process causes amorphization. The absorption spectra indicate that lower and middle fluence irradiation reduce the bandgap, while the highest fluence increases it. The pristine film has spherical nanostructures as revealed from the AFM image. The lowest and middle fluence irradiation increases the size and rms roughness of the surface nanostructures but the highest fluence irradiation makes the nanostructures vanish, resulting in lower surface roughness. The current-voltage (I-V) characteristics show that irradiation consistently decreases electrical conductivity. The changes in structural, optical, surface morphological, and electrical properties due to irradiation are correlated to the high energy deposited through electronic energy loss using thermal spike model.

Keywords: TiO₂ thin films, Swift Heavy Ion Irradiation, XRD, UV-Vis, AFM, I-V Characteristics

1. Introduction

Titanium dioxide (TiO₂) is a wide band gap n-type semiconductor material which belongs to the transition metal oxides family. It is found in three crystallographic forms in nature: rutile, anatase and brookite. Rutile and anatase have tetragonal while brookite has orthorhombic structure. At normal temperature and pressure, rutile is thermodynamically stable while anatase and brookite are metastable in the bulk form. Zhang and Banfield [1] have concluded that the thermodynamic stability of rutile and anatase reverses in nano regime i.e. anatase phase becomes more stable than rutile when particle size approaches at ~14 nm. Nevertheless, particle size is not the sole determinant of the thermal stability of anatase and rutile phases. Post-deposition processes such as annealing and ion irradiation, specifically utilizing swift heavy ions (SHI), can be employed to alter the phases of metal oxide nanoscale thin films [2]. The phase

generation of titanium oxide mainly depends on the synthesis process. Typically, it has been observed that the primary crystalline phase in various deposition techniques is anatase. However, there is also a possibility of rutile phase formation under conditions close to room temperature [1-5].

Thin films and nanostructures of titanium oxide have been deposited and studied by many researchers in its doped and undoped form over the last few decades because of its wide range of applications due to its unique optical, electronic and structural properties [6,7]. Photocatalysis, white pigmentation, dye sensitized solar cells (DSSCs), antimicrobial, anti-reflective and self-cleaning coatings, gas sensors, photoelectrochemical cells (PECs), air and water purification are some important applications of titanium oxide. In addition to these applications, nano-scale titanium oxide has gained significant attention because of its low cost, chemical stability and minimal toxicity [6-14]. Numerous reports indicate that distinct phases of titanium oxide exhibit varying properties that render them appropriate for specific categories of applications [1,3,4,15-17]. Considering the significant volume of applications, a variety of deposition methods have been utilized to enhance the properties and functionality of devices based on different phases, nano-scale particle sizes, shapes and morphology of titanium oxide. Each deposition route or method comes with its own set of advantages and disadvantages. Chemical route has the chance to produce residues and contaminants within the films which could have detrimental effects on the quality and functionality of the deposited films [18]. The technology of physical vapour deposition (PVD) remains a prevalent method for producing functional coatings. Various PVD techniques have been employed for the deposition of titanium oxide nano thin films in order to enhance their characteristics and optimize device functionality including thermal evaporation [19], RF magnetron sputtering [20,21], e-beam evaporation method [22,23], and pulsed laser deposition (PLD) [24-26]. The PLD technique offers numerous benefits, notably the ability to regulate stoichiometry, particularly in materials with intricate compositions. It also allows for the creation of adherent coatings, easily obtainable multi-layered thin films, flexible experimental design, and control over morphology and crystallinity. Additionally, adjusting the deposition conditions enables customization of the composition-structure-properties relationship of the films. The high-energy photons emitted by the laser do not induce any form of contamination in the films [27,28].

Swift heavy ion (SHI) has emerged as a preferred method for customizing the properties of thin films to achieve specific characteristics and optimize device functionality [2,29]. Energetic ions experience depth-dependent energy depletions as they traverse through a material, resulting from elastic interactions with the nuclei of the target material and inelastic interactions with its electronic structure. These energy depletions are referred to as nuclear (S_n) and electronic energy losses (S_e), respectively. The energy stored in the electron excitations becomes interconnected with the lattice, leading to the transmission of energy from electrons to lattice system. This process can result in the formation of a highly stimulated cylindrical region measuring a few nanometers in lateral dimensions along the path of the ion and material is modified [2, 29]. Ishikawa et al. [30] irradiated anatase titanium oxide thin films grown by PLD on STO substrates by 230 MeV Xe and 200 MeV Au ions. The plane indexed as (004) decreased exponentially as a function of ion fluence. Thakurdesai et al. [31] studied nano-hillocks formation on the surface of titanium oxide thin films

due to the irradiation. They prepared amorphous thin films by PLD method and irradiated using 100 MeV Ag ions at different fluences and found irradiation induced phase transformation (amorphous to anatase) along with hillocks formation on the surface which was initially smooth. Thakur et al. [32] report the modifications in structural and electronic properties of titanium oxide thin films deposited by R F magnetron sputtering method using 200 MeV Ag ions. They obtained structural phase transition from anatase to admixture of brookite and rutile phases of TiO_2 with increasing fluence followed by a significant distortion in the TiO_6 octahedra. O'Connell et al. [33] studied temperature dependence of SHI irradiation induced hillocks formation in TiO_2 . Irradiation was performed by 220 MeV Xe ions at different temperature ranges from 80 K to 1000 K and found that average hillock height increased with irradiation temperature. All hillocks were found to be crystalline and epitaxial with the original crystal surface. Zhai et al. [34] reported the first observation of fine structure of latent tracks in rutile TiO_2 , which changes from cylinder to dumbbell-shape and then to sandglass-shape as a function of the ion path length. Moreover, the cone length of the track was found to be dependent on electronic energy loss. The results indicate that outflow of the thermal spike-induced molten phase produces the hillocks on surface and the void-rich zone near surface after epitaxial recrystallization due to material deficit, while at a deep depth, the lack of efficient outflow and recrystallization result in the absence of tracks. They concluded that the various morphologies of tracks in rutile TiO_2 are a consequence of the molten phase outflow and recrystallization during rapid cooling down. In the present study, the nanocrystalline titanium oxide (TiO_2) thin films are prepared using PLD technique on both quartz and Si substrates and exposed to 120 MeV Au ions at different fluences to study the irradiation induced modifications.

2. Experimental details

Nanocrystalline TiO_2 thin films were fabricated on Si (1 0 0) and quartz substrates utilizing the PLD technique at UGC -DAE CSR Indore. Prior to the film deposition, the substrates underwent ultrasonic cleaning for a duration of three minutes. A pellet was prepared from commercially available TiO_2 powder with a purity of 99.99% (Sigma Aldrich). The pellet had an approximate diameter and thickness of 1.6 inches and 5 mm, respectively. The pellet was subjected to sintering at 1000 °C for eight hours before being utilized as the target material. The meticulously cleaned substrates were affixed onto substrate holders, and the deposition chamber was evacuated to a base pressure of 5×10^{-5} Torr. Oxygen gas was introduced into the deposition chamber to maintain a deposition pressure of 1×10^{-3} Torr. The deposition process involved utilizing KrF radiation (wavelength 248 nm) emitted by a Lambda Physik LPX excimer laser focused on a rotating target. The energy delivered by each laser pulse to the target amounted to 220 mJ, with a repetition rate of 10 Hz and a total deposition time of ~30 minutes. During the process, the substrate temperature was carefully regulated at 630 °C, while maintaining an approximate distance of ~5 cm between the target and substrate. The thickness of the film was subsequently measured using profilometry techniques, revealing it to be approximately 90 nm in magnitude.

Irradiation was conducted using 120 MeV Au ions at various fluences ranging from 1×10^{11} to 1×10^{13} ions/cm² utilizing the 15 UD tandem pelletron accelerator at the Inter University Accelerator Centre

(IUAC), New Delhi. The irradiation chamber was evacuated to a base pressure of 10^{-6} Torr. Irradiations were carried out at room temperature and perpendicular to the surface of the films. The ion flux was maintained at a low level to minimize charging effects and sample heating. The electronic energy loss (S_e) and nuclear energy loss (S_n) in TiO_2 for 120 MeV Au ions were determined as 22.95 keV/nm and 0.32 keV/nm, respectively, using Stopping and Range of Ions in Matter (SRIM) software [35]. The projected range was calculated to be 10.40 μm . It is evident that S_e outweighs S_n multiple times, indicating that any modifications or defects in the film are likely due to S_e -related mechanisms exclusively. Furthermore, since the projected range exceeds the film thickness of 90 nm, the possibility of ion implantation can be ruled out. Consequently, any modifications or defects are anticipated to arise solely from the S_e -induced process during ion passage through the film.

The pristine and irradiated films were analyzed utilizing X-ray diffraction (XRD), UV-Vis spectroscopy, and atomic force microscopy (AFM) techniques to investigate their structural, optical, and surface morphological properties. XRD patterns were obtained using a Brooker-D8 advanced AXS diffractometer ($\text{Cu K}\alpha_1$, 1.54 \AA) at a grazing angle of 2° with a scanning rate of $0.5^\circ \text{ min}^{-1}$. The UV-Vis absorption spectra were recorded with a Hitachi U-3300 spectrophotometer in the wavelength range of 200 to 800 nm. AFM images were taken using Nanoscope IIIA scanning probe microscope operating in tapping mode. Current -Voltage (I-V) characteristics were recorded at room temperature using Keithley source meter (2400). These analyses were carried out at IUAC New Delhi and R.B.S. College, Agra.

3. Results and discussion

3.1 XRD Results

Figure -1 illustrates the XRD pattern of both pristine and irradiated TiO_2 thin films deposited on Si (100) substrate.

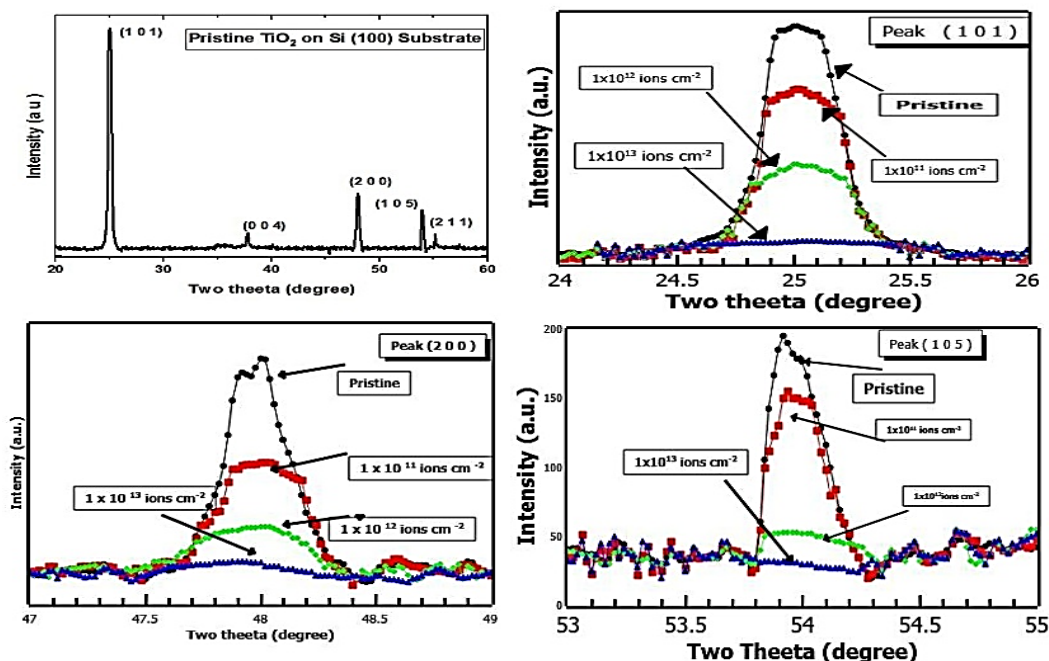


Figure-1: XRD Pattern of Pristine and Irradiated films on Si substrate

The pristine film is identified as a polycrystalline film and displaying the tetragonal anatase phase with peak positions consistent with the anatase structure. This film demonstrates a preferred orientation along the (101) plane, which is recognized as the most thermodynamically stable plane. The average crystallite size (CS) was determined using Scherrer's formula [36] yielding a value of 9.89 nm. Upon irradiation at varying fluences, a continuous decrease in crystallinity is observed, as indicated by the XRD pattern. At the lowest fluence of 1×10^{11} ions/cm², the average crystallite size (CS) is measured at 6.69 nm, while at the intermediate fluence of 1×10^{12} ions/cm², it further reduces to 2.16 nm. Notably, no diffraction peaks are detected at the highest fluence of 1×10^{13} ions/cm², suggesting a transition to amorphization.

The possible explanation of this kind of structural modification induced by 120 MeV Au ions can be given using thermal spike model [29-34]. When energetic heavy ion passes through the material, it deposits large amount of energy into the material. This energy is deposited by the projectile ions in the electronic subsystem of the material. This energy is shared among the electrons and then transferred subsequently to the lattice via electron-lattice interactions, leading to a large increase in the temperature along and in the vicinity of the ion path. Pressure waves develop due to the temperature spike and cause strain in the nanosized structure. The process of energy transfer from energetic ions to material takes place in $\sim 10^{-14}$ s. Such extremely short and intense solid -state excitations, localized in a nano-scale volume, generate non-equilibrium phases. This non-equilibrium phase results modifications in the material. At low fluence (1×10^{11} ions/cm²) irradiation, energetic Au ion can create the latent track along its trajectory because its S_e (=22.95 keV/nm) is much greater than the reported value of threshold of latent track formation S_{eth} (=6.2 keV/nm) [31,32]. At this fluence, the material may not be disturbed too much and maintain some crystallinity. At middle fluence irradiation (1×10^{12} ions/cm²), the multiple ion tracks begin to overlap, increasing the lattice disorder and pushing the material into amorphous state. At the highest fluence (1×10^{13} ions/cm²) irradiation, the progressive disordering process takes place causing the destruction of long-range crystalline order and making the film amorphous.

Reports indicate that materials undergo amorphization when subjected to irradiation. Ishikawa et al. [30] has observed the exponential decrement of XRD peak of (004) plane of anatase TiO₂ after irradiation with 230 MeV Xe ions and 200 MeV Au ions at different fluences. Hazem et al. [37] prepared anatase TiO₂ thin films using the sol-gel method and subsequently irradiated these films with 25.8 MeV Cu ions ($S_e = 10.3$ keV/nm) and 90 MeV Xe ions ($S_e = 20.3$ keV/nm) at varying fluences, demonstrating a loss of crystallinity due to irradiation. Additionally, Abushad et al. [38] recently reported partial amorphization in anatase TiO₂ thin films grown by PLD following irradiation with 100 MeV Ag ions. In our previous work [39], we observed the occurrence of amorphization in tin oxide thin films grown by PLD when subjected to irradiation with 100 MeV Ag ions at liquid nitrogen temperature.

3.2 AFM Results

Surface morphologies of the pristine and irradiated films by 120 MeV Au ions are shown in Figure-2. The morphology of the pristine film is showcasing nanostructures of TiO₂ with predominantly spherical shapes and size distribution ranging from 60 to 140 nm, with an average size of surface nanostructures

(nanospheres) ~ 100 nm. The root mean square (rms) surface roughness measures at 1.6 nm. Exposure to ion doses of 1×10^{11} and 1×10^{12} ions cm^{-2} resulted in an increase in the size of the nanostructures, with rms surface roughness rising to 4.31 and 6.30 nm respectively. Despite this growth, the spherical shape remained unaltered, yet the average grain size expanded to 186 and 203 nm correspondingly.

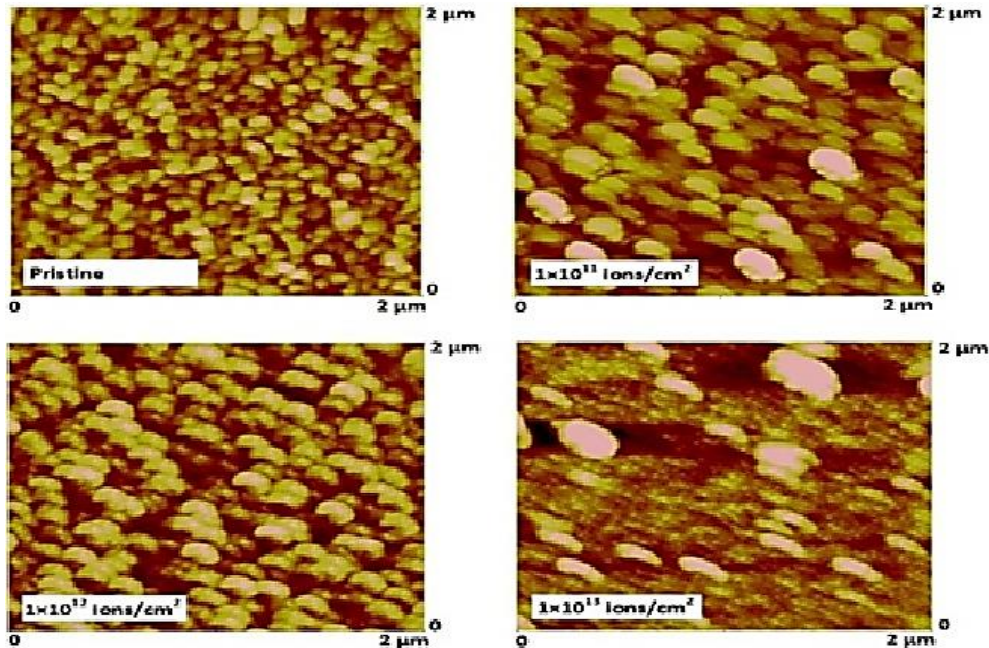


Figure-2: The AFM micrographs of Pristine and irradiated films

Irradiation at the highest fluence 1×10^{13} ions cm^{-2} , the spherical nanostructures have ceased to exist, and only large clusters are observable, exhibiting a surface roughness of 5.09 nm. The size distributions of the synthesized nanostructures are presented in Figure - 3. The low rms surface roughness (1.6 nm) observed in the as-deposited film may be attributed to the slower sputtering rate during deposition, leading to a more uniform distribution of small grains on the surface and consequently lower roughness. Irradiation triggers the agglomeration of smaller nanostructures into large structures, causing an increase in surface roughness. This outcome also indicates that the irradiation does not alter the shape of the grains. This phenomenon is likely attributed to the fragmentation of the TiO_2 crystallites and their subsequent agglomeration during the transit of ions through the film. Upon exposure to the highest fluence irradiation, the film has transitioned into an amorphous state, resulting in the random agglomeration of material on its surface.

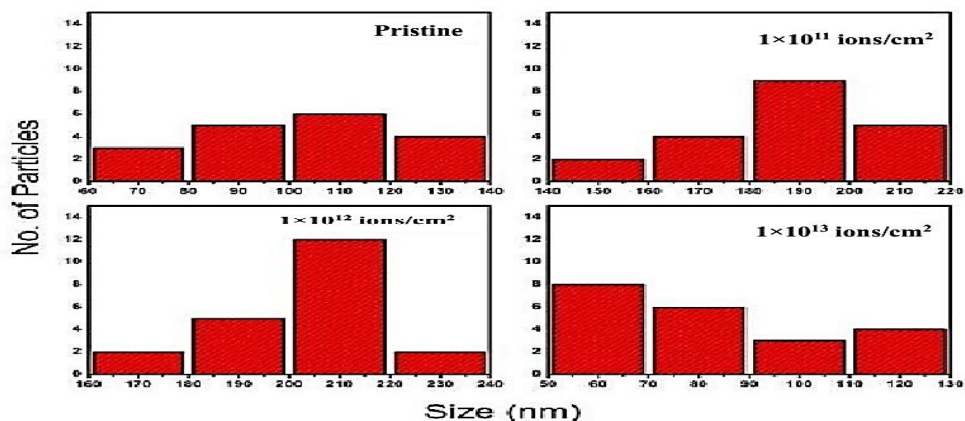


Figure-3: The size distribution of surface nanostructures

RMS roughness is a widely used metric for characterizing surface morphology, reflecting the average height deviations of a surface from its mean value. Surface roughness is a crucial factor that affects the durability and performance of materials. In the context of thin films and semiconductor devices, surface roughness plays a key role in enhancing electrical properties, adhesion, and particle capture capabilities, among other features [40]. The roughness of surfaces can significantly alter the properties of devices based on thin films. Consequently, evaluating and controlling surface roughness is essential to ensure that these devices meet their intended electrical, thermal, optical, mechanical, and chemical function. Roughness measurements obtained through AFM are represented by basic statistical parameters such as average roughness and RMS roughness, which are conveyed as single values. However, this can lead to identical roughness measurements for surfaces with vastly different morphologies. This overlap in roughness values across diverse surface structures occurs because these roughness algorithms are not sensitive to lateral features. Research has shown that roughness values derived from statistical theories are highly dependent on factors such as sampling interval, scanning scale, randomness of the measured areas, and the specifics of each measurement technique [41,42].

A more detailed characterization of surface is attained through the power spectral density (PSD) of the surface topography. Unlike traditional statistical analyses, the PSD algorithm has demonstrated effectiveness in describing various intricate surface geometries and in elucidating the influence of surface morphology on the properties of material systems. The PSD breaks down the surface profile into its spatial wavelengths, enabling the comparison of roughness measurements across different spatial frequency ranges. This function is particularly important for optical surfaces and is widely used for evaluating surface quality. It has its direct relationship with the quantity and angular distribution of scattered light. The scattering theories indicate that for smooth surfaces, the angular distribution of scattered light from a surface corresponds with the PSD of the surface topography [40-42]. The PSD analysis was undertaken in order to get information about the roughness exponent and the processes which are responsible for the surface evolution under 120 MeV Au irradiation. The 2D-PSD function is a Fourier transform of the surface which is defined as below [43,44]

$$\text{PSD} = \frac{1}{A} \left[\iint \frac{d^2 r}{2\pi} \exp(-iqr) \langle h(r) \rangle \right]^2 \quad (1)$$

Where A represents the scanned area, q is the spatial frequency (here in μm^{-1}) and h(r) represents the surface height at the point r (x,y).

$$\text{PSD} = Kq^{-m} \quad (2)$$

K represents the constant of proportionality, while m denotes the power law exponent. The exponent m characterizes the mechanism that governs surface evaluation. To determine the value of m, a linear fit is applied to the straight-line segment (high-frequency region) of the PSD curves. The slope derived from this linear fit corresponds to the value of m. Following the determination of m, the roughness exponent (α) is calculated using the formula $\alpha = (m-d)/2$, where d equals 2 for 2D-PSD.

The values of slope (m) and roughness exponent (α) of the pristine and irradiated films are given in Table-1 and PSD curves are shown in Figure-4. Since the value of m lies between 3.72 to 3.86, the observed surface evaluation in this case is due to volume and surface diffusion. The value of α is less than 1, which is the condition for the self-affine nature of the structures induced by SHI irradiation [43].

Table-1 Value of Roughness exponent

| S.No. | Ion Fluence (ion/cm ²) | Slope (m) | Roughness Exponent (α) |
|-------|------------------------------------|---------------|---------------------------------|
| 1. | Pristine | 3.72 | 0.86 |
| 2. | 1×10^{11} | 3.78 | 0.89 |
| 3. | 1×10^{12} | 3.85 | 0.92 |
| 4. | 1×10^{13} | 3.86 | 0.93 |

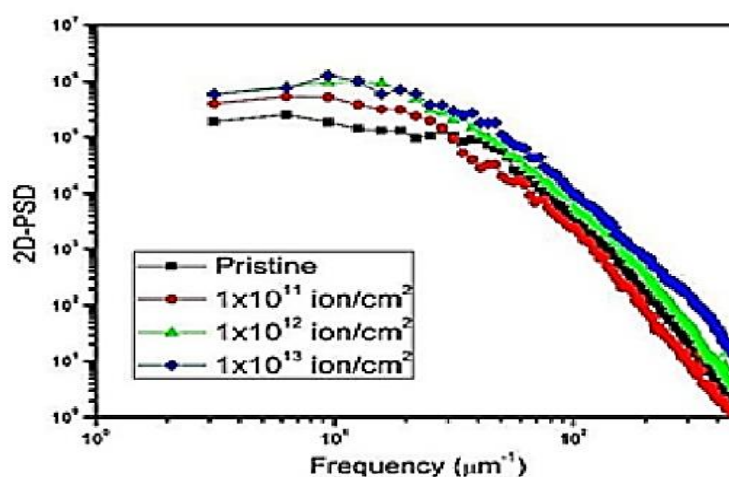


Figure-4: 2D-PSD curves of pristine and irradiated films

The extremely short and intense solid-state excitations induced by irradiation, which are localized within a nanoscale volume, give rise to non-equilibrium phases characterized by unique structural and physical properties at the nanometer scale. These properties can serve as a foundation for the development of functional nanostructures. Increasing the ion fluence and the number of modified zones, the interaction and finally the overlap of these zones give rise to surface instabilities and self-organization effects. In 'self-organization' a system develops some kind of structuring by itself, that is, without selective intervention from outside. Such instabilities in thin film systems can be triggered by energetic ion bombardment and the subsequent self-assembly of the surface can be controlled by fine-tuning of the irradiation conditions [31,43,44].

In the present study, the value of Se is 22.95 keV/nm which is much greater than Se threshold ($S_{eth} = 6.2$ keV/nm) for TiO_2 [31,32]. This value of Se will create amorphized zone along the ion track in the film and in the very short period of time ($\sim 10^{-14}$ s) the melting of material and fusion will take place. Due to the fusion, bigger nanostructures are developed. This destabilizes the crystal structure and make the material amorphous. Increasing the ion fluence, the material becomes completely amorphized and randomly distributed big clusters are obtained. The XRD results also supports the AFM results.

3.3 UV-Vis Results

Figure-5 shows the absorption spectra of pristine and irradiated films deposited on quartz substrates and figure-6 shows the variation of band gap E_g with ion fluence. The band gap has been estimated using Tauc's procedure [43].

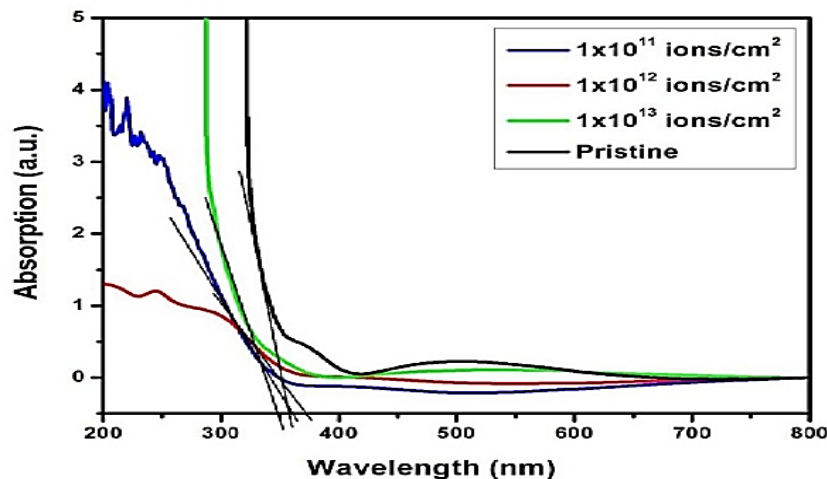


Figure-5: Absorption spectra of pristine and irradiated films on quartz substrate

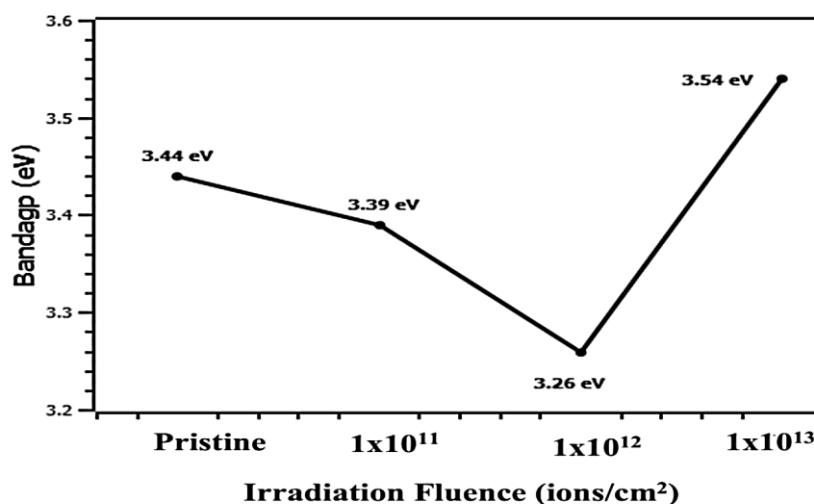


Figure-6: Variation of bandgap with fluence

The bandgap of pristine film is estimated to be ~ 3.44 eV which is a little greater than its generally accepted values 3.2 eV (anatase) and 3.0 eV (rutile) at room temperature [7,12]. The optical band gap is affected by many parameters such as deposition methods, crystallinity, surface roughness, morphology and films thickness etc. In nano regime, surface to volume ratio increases which causes self-equilibrium state of nanostructures and the excess energy of surface atoms influences the band structure. This excess surface energy can significantly influence the band structure of the nanomaterials. Essentially, the band gap can become wider in nanoscale materials compared to their bulk counterparts because the electrons are more confined in a smaller volume, leading to higher energy states. The value of band gap decreases to ~ 3.39 eV from ~ 3.44 eV on the lowest fluence (1×10^{11} ions/cm²) which further drops to ~ 3.26 eV at the middle fluence (1×10^{12} ions/cm²) irradiation. However, at the highest fluence (1×10^{13} ions/cm²) irradiation, bandgap shows an increase (~ 3.54 eV) close to pristine film value. Decrease of bandgap (E_g) at the lowest

and middle fluence regime is possibly due to lattice distortion resulting in the generation of a number of shallow energy levels in TiO_2 . One of the reasons of SHI induced lattice distortion is oxygen loss [45]. The oxygen loss may occur within and around the ion tracks with varying degrees upto the middle fluence (1×10^{12} ions/cm²) irradiation. The increase of bandgap is observed at the highest fluence (1×10^{13} ions/cm²), where the ion tracks are expected to overlap and drive the TiO_2 towards an amorphous state beyond a critical defect concentration. Such a disordered state can contribute to the increase of bandgap at high ion fluences [46-51].

3.4 I-V Characteristics Study

The electrical properties of both pristine and irradiated films are examined through a systematic measurement of current as the function of voltage. The I-V characteristics of pristine and irradiated films are shown in Figure-7. The pristine film shows good electrical conductivity, as evidenced by the I-V plots, which indicate a linear relationship between current and voltage. This conductivity can be attributed to the efficient movement of charge carriers within the material, facilitated by a well-ordered crystalline structure that minimizes scattering events of charge carriers. Since the film is deposited in oxygen-rich environment, the charge carrier concentration will be relatively low in pristine film. Presence of the oxygen can act as a trap for charge carriers, effectively reducing their concentration within the film. As a result, the electrical conductivity observed in the pristine film may primarily be attributed to the high mobility of the existing charge carriers [39,52].

When the film undergoes irradiation at different fluences, a monotonic transformation (from crystalline to amorphous) is seen that has profound implications for the behavior of charge carriers within the material in thin film. In the amorphous structure, there is lack of long-range order that disrupts the pathways of charge carriers and thus reduction in the current is obtained. Irradiation generated various types of defects, including vacancies, interstitials, and dislocations can increase the carrier concentration by providing additional states for electrons to occupy. This increase in carrier concentration can enhance the material's conductivity. However, the same defects can also scatter charge carriers, which leads to a reduction in their mobility. The interplay between increased carrier concentration and decreased mobility is crucial in determining the overall electrical properties of the material.

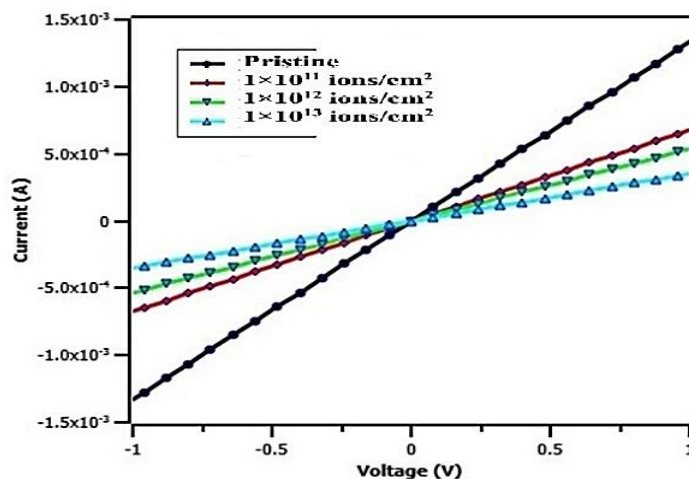


Figure-7: variation of electric current with dc voltage

In the present case, it is believed that the amorphous state has disrupted the charge carriers and irradiation induced various defects has scattered them leading to reduction in conductivity [52-55].

4. Conclusions

The present study demonstrates that 120 MeV Au ions significantly alter the structural, optical, morphological, and electrical properties of PLD grown nanocrystalline TiO₂ thin films. XRD analysis confirms a systematic transition from a polycrystalline to an amorphous phase with increasing ion fluence. Optical studies reveal a non-linear trend in bandgap modification, with decrease up to middle fluence followed by an increase at the highest fluence irradiation. AFM analysis highlights the evolution of surface morphology, showing increased nanostructure size and surface roughness upto middle fluence irradiation, while the highest fluence leads to the disappearance of spherical nanostructures and the formation of large clusters having decreased roughness. Electrical measurements indicate a linear trend showing decrease in conductivity with irradiation fluences.

References

- [1]. Hengzhong Zhang and Jillian F. Banfield, *J. Mater. Chem.*, **8(9)**, 2073 (1998).
- [2]. N C Mishra, *Radiation Effects and Defects in Solids* 166(8-9), 657 (2011).
- [3]. D J Won, C H Wang, H K Jang and D J J. Choi, *Applied Physics A* **73**, 595 (2001).
- [4]. Dorian A. H. Hanaor and Charles C. Sorrell, *J. Mater. Sci.* **46**, 855 (2011).
- [5]. Joseph Muscat, Varghese Swamy, and Nicholas M. Harrison, *Phys. Rev. B* **65**, 224112 (2002).
- [6]. S.J. Armaković, M.M. Savanović, S. Armaković, *Catalysts*, **13(1)** 26, (2023).
- [7]. Anuel Jesús Gázquez, Silvia María Pérez Moreno, Juan Pedro Bolívar, *Metal Oxides*, Elsevier, (2021), ISBN 9780128199602, pp.311-335.
- [8]. Y. Akila, N. Muthukumarasamy, Dhayalan Velauthapillai, *Nanomaterials for Solar Cell Applications*, Elsevier, (2019), ISBN 9780128133378, pp.127-144.
- [9]. Chi-Jen Chung, Hsin-I Lin, Hsi-Kai Tsou, Zhi-Yuan Shi, Ju-Liang He, *Journal of biomedical materials research. Part B, Applied biomaterials*, **85(B)** (2008) 220-224.
- [10]. Li Tian, Ling Li, Min Wu, *Micro Nano Lett.*, **(12)**, 849 (2017).
- [11]. Nisha T. Padmanabhan, Honey John, *Journal of Environmental Chemical Engineering*, **(8) 5**, 104211 (2020).
- [12]. Xu Tian, Xiuxiu Cui, Tingrun Lai, Jie Ren, Zhichao Yang, Mingjing Xiao, Bingsen Wang, Xuechun Xiao, Yude Wang, *Nano Materials Science*, **3(4)**, 390 (2021).
- [13]. Anna Kusior, Anna Wnuk, Anita Trenczek-Zajac, Katarzyna Zakrzewska, Marta Radecka, *International Journal of Hydrogen Energy*, **40(14)**, 4936 (2015).
- [14]. Vassilios Binas, Danae Venieri, Dimitrios Kotzias, George Kiriakidis, *Journal of Materiomics*, **3(1)**, 3 (2017).
- [15]. Adawiyah J. Haider, Zainab N. Jameel, Imad H.M. Al-Hussaini, *Energy Procedia* ,**157**, 17(2019).
- [16]. Xiaobo Chen and Samuel S. Mao, *Chemical Reviews*, **107(7)**, 2891 (2007).
- [17]. Shang-Di Mo and W. Y. Ching, *Phys. Rev. B*, **51**, 130231995 (1995).

- [18]. Olayinka Oluwatosin Abegunde, Esther Titilayo Akinlabi, Oluseyi Philip Oladijo, Stephen Akinlabi, Albert Uchenna Ude, *AIMS Materials Science* **6(2)**,174 (2019).
- [19]. R.S. Dariani, Z. Nafari Qaleh, *Thin Solid Films*, **542**,192 (2013).
- [20]. Cheol Ho Heo, Soon-Bo Lee, Jin-Hyo Boo, *Thin Solid Films*, **475(1,2)**, 183(2005).
- [21]. Stanislav Mráz, Jochen M. Schneider, *J. Appl. Phys.*, **109(2)**,023512 (2011).
- [22]. M.H. Mangrola, V.G. Joshi, *Materials Today: Proceedings* 4(2),3832, (2017).
- [23]. Min Wook Pyun, Eui Jung Kim, Dae-Hwang Yoo, Sung Hong Hahn, *Applied Surface Science*, **257(4)**, 1149 (2010).
- [24]. A.K Sharma, R.K Thareja, Ulrike Willer, Wolfgang Schade, *Applied Surface Science*, **206(1-4)**, 137 (2003).
- [25]. D. Dzibrou, A.M. Grishin, H. Kawasaki, *Thin Solid Films*, **516(23)**, 8697 (2008).
- [26]. E György, A Pérez del Pino, G Sauthier, A Figueras, F Alsina and J Pascual, *J. Phys. D: Appl. Phys.* **40**, 5246 (2007).
- [27]. Dave H A Blank, Matthijn Dekkers and Guus Rijnders, *J. Phys. D: Appl. Phys.* **47**, 034006 (2014).
- [28]. Emanuel Axente and Gabriel Socol, *Coatings*, **12(3)**, 368 (2022).
- [29]. D.K. Avasthi, *Curr. Sci.* **78(11)**, 1297 (2000).
- [30]. N. Ishikawa, S. Yamamoto, Y. Chimi, *Nucl. Instr. Meth. Phys. Res. B* **250(1-2)**, 250 (2006).
- [31]. Madhavi Thakurdesai, D. Kanjilal, Varsha Bhattacharyya, *Applied Surface Science* **254(15)**, 4695 (2008).
- [32]. Hardeep Thakur, Ravi Kumar, P. Thakur, N. B. Brookes, K. K. Sharma, Abhinav Pratap Singh, Yogesh Kumar, S. Gautam, K. H. Chae; *J. Appl. Phys.* **110(8)**, 083718 (2011).
- [33]. J H O'Connell, G Aralbayeva, V A Skuratov, M Saifulin, A Janse van Vuuren, A Akilbekov and M Zdorovets, *Mater. Res. Express* **5(5)**, 055015 (2018).
- [34]. Pengfei Zhai, Shuai Nan, Lijun Xu, Weixing Li, Zongzhen Li, Peipei Hu, Jian Zeng, Shengxia Zhang, Youmei Sun, Jie Liu, *Nucl. Instr. Meth. Phys. Res. B*, **457**, 72(2019).
- [35]. J.F. Ziegler, M.D. Ziegler, J.P. Biersack, Stopping and Ranges of Ions in Matter, SRIM Code (<http://www.srim.org/>)
- [36]. D.C. Agarwal, R.S. Chauhan, Amit Kumar, D. Kabiraj, F. Singh, S.A. Khan, D.K. Avasthi, J.C. Pivin, M. Kumar, J. Ghatak, P.V. Satyam, *J. Appl. Phys.* **99**, 123105 (2006).
- [37]. R. Hazem, M. Izerrouken, A. Sari, S. Kermadi, M. Msimanga, A. Benyagoub, M. Mazza, M. Belgaid, M. Boumaour, *Nucl. Instr. Meth. Phys. Res. B*, **3.4**, 16(2013).
- [38]. M. Abushad, M. Arshad, Fouran Singh, R.J. Choudhary, Manoj Kumar, Bushara Fatma, Azizurrahman Ansari, Shahid Husain, Wasi Khan, *Radiation Physics and Chemistry*, **216**, 111371 (2024).
- [39]. R S Chauhan, Vijay Kumar, Anshul Jain, Deepti Pratap, D C Agarwal, R J Chaudhary, Ambuj Tripathi, *Adv. Mat. Lett.* **5(11)**, 666(2014).

- [40]. R. Gavrilă, A. Dinescu, D. Mardare, *Romanian Journal of Information Science and Technology*, **10(3)**, 291 (2007).
- [41]. Yuxuan Gong, Scott T. Mixture, Peng Gao, Nathan P. Mellott, *J. Phys. Chem. C*, **120**, 22358 (2016).
- [42]. D. Franta, I. Ohlídal, P. Klapetek, P. Pokorný, *Surf. Interface Anal.*, **34**, 759 (2002).
- [43]. D.C. Agarwal, R.S. Chauhan, D.K. Avasthi, S.A. Khan, D. Kabiraj, *J. Appl. Phys.*, **104**, 024304(2008).
- [44]. Vijay Kumar, Anshul Jain, Deepti Pratap, D.C. Agarwal, A. Tripathi, R.S. Chauhan, *Radiation Effects & Defects in Solids*, **168(7-8)**, 490 (2013).
- [45]. R.R. Mohanta, V.R.R. Medicherla, K.L. Mohanta, Nimai C. Nayak, S. Majumder, V. Solanki, Shikha Varma, Komal Bapna, D.M. Phase, V. Sathe, *Applied Surface Science*, **325**, 185 (2015).
- [46]. Haripriya Rath, B.N. Dash, A. Benyagoub, N.C. Mishra, *Scientific Reports*, **8**, 11774 (2018).
- [47]. Avesh Kumar, M.K. Jaiswal, D. Kanjilal, Rakesh K. Joshi, T.Mohanty, *Appl. Phys. Lett.* **99**, 013109(2011).
- [48]. Nishad G. Deshpande, Ramphal Sharma, *Current Applied Physics*, **8**, 181 (2008).
- [49]. R.S. Chauhan, Vijay Kumar, D.C. Agarwal, Deepti Pratap, I. Sulania, A. Tripathi, *Nucl. Instrum. Methods Phys. Res. B* **286**, 295 (2012).
- [50]. Nagaraj G., Dhayal Raj A., Albert Irudayaraj A., Josephine R.L., *Optik*, **179**, 889 (2019).
- [51]. Xinchun Mao, Xiufeng Lang, Zhiqiang Wang, Qunqing hao, Bo Wen, Zefeng Ren, Dongxu Dai, Chuanyao, Li-Min Liu, Xueming Yang, *J. Phys. Chem. Lett.* **4**, 3839(2013).
- [52]. Fei Cao, Gerko Oskam, Gerald J. Meyer, Peter C. Searson, *The Journal of Physical Chemistry*, **100(42)**, 17021 (1996).
- [53]. H. Tang, K. Prasad, R. Sanjines, P.E. Schmid, F. Levy, *J. Appl. Phys.* **75**, 2042(1994).
- [54]. Paul Nunez, Matthias H. Richter, Brandon D. Piercy, Christopher W. Roske, Miguel Caban-Acevedo, Mark D. Losgego, Steven J. Konezny, David J. Fermin, Shu Hu, Bruce S. Brunshwig, Nathan S. Lewis, *The Journal of Physical Chemistry*, **123(33)**, 20116(2019).
- [55]. Wanheng Lu, Lai-Mun Wong, Shijie Wang, Kaiyang Zeng, *Journal of Materiomics*, **4(3)** 228(2018).

Cite this Article

Vijay Kumar, D.C. Agarwal, R.S. Chauhan, "Modification of PLD Grown Nano TiO₂ Thin Films using 120 MeV Au Ion Irradiation", *International Journal of Multidisciplinary Research in Arts, Science and Technology (IJMRASST)*, ISSN: 2584-0231, Volume 3, Issue 6, pp. 11-23, June 2025.

Journal URL: <https://ijmrast.com/>

DOI: <https://doi.org/10.61778/ijmrast.v3i6.140>



This work is licensed under a [Creative Commons Attribution-NonCommercial 4.0 International License](https://creativecommons.org/licenses/by-nc/4.0/).